Available online at www.sciencedirect.com
ScienceDirect
Journal of Molecular Catalysis A: Chemical 268 (2007) 195–200
JOURNAL OF MOLECULAR CATALYSIS A: CHEMICAL
www.elsevier.com/locate/molcata

Ultrasonic-assisted synthesis of visible-light-induced Bi_2MO_6 (M = W, Mo) photocatalysts

Lin Zhou, Wenzhong Wang *, Lisha Zhang

State Key Laboratory of High Performance Ceramics and Superfine Microstructure, Shanghai Institute of Ceramics, Chinese Academy of Sciences, 1295 DingXi Road, Shanghai 200050, PR China

Received 31 October 2006; received in revised form 7 December 2006; accepted 10 December 2006
Available online 21 December 2006

Abstract

Visible-light-induced photocatalysts Bi_2MO_6 (M = W, Mo) nanocrystals have been successfully synthesized via a new ultrasonic-assisted method. Laminar structured Bi_2WO_6 nanoplates with size of *ca.* 100 nm and Bi_2MoO_6 nanoparticles with size of *ca.* 150 nm were prepared via ultrasonic pretreatment followed by calcination at 500 °C. The photocatalytic activities of as-prepared Bi_2MO_6 were about 4–6 times higher than that of the products prepared by traditional solid-state reaction (SSR), which were evaluated by the degradation of RhB dye in water under visible light irradiation ($\lambda > 400$ nm). It was found that ultrasonic irradiation played an important role in the formation of the nanomaterials with a smaller crystal size and larger surface area, which was beneficial to their photocatalytic activities. The present study suggested a promising method, as an effective improvement of traditional SSR-process, for the synthesis of other photocatalysts.

Keywords: Bi_2MO_6 (M = W, Mo); Photocatalysis; Ultrasonic; Visible light; RhB

1. Introduction

From the viewpoint of solving global energy and environment issues, using solar energy and semiconductors as catalysts for photocatalytic degradation of harmful pollutants and water splitting have attracted great interest in recent years [1–3]. Considering the relatively slow reaction rate and poor solar efficiency of TiO_2 which hindered its application, many studies have been carried out to exploit new visible-light-driven photocatalysts. Zou et al. [4] have firstly reported water splitting for H_2 and O_2 evolution in a stoichiometric amount over the $NiO_x/In_{0.9}Ni_{0.1}TaO_4$ photocatalyst under visible light irradiation. Since then, some other new visible-light-induced photocatalysts have also been developed [5–10], besides TiO_2 based photocatalysts. Bismuth mixed oxides $(Bi_2O_2)^{2+}$ $(A_{n-1}B_nO_{3n+1})^{2-}$ (A = Ba, Bi, Pb, etc., B = Ti, Nb, W, Mo, etc.) with Aurivillius structure are an important set of visible-light active photocatalysts for environmental purification and/or water splitting [11,12]. These bismuth containing oxides possess unique layered structures by the perovskite slabs of $(A_{n-1}B_nO_{3n+1})^{2-}$ sandwiched between $(Bi_2O_2)^{2+}$ layers. Among them, Bi_2WO_6 and Bi_2MoO_6 have been reported by Kudo and his co-workers [13,14] as photocatalysts for O_2 evolution from $AgNO_3$ solution. Lately, Bi_2WO_6 was demonstrated to show activity for degradation of organic pollutants [15,16]. Even so, it is still of great importance and challenge to explore bismuth mixed oxides photocatalysts with high efficiency and visible light responsibility.

Traditionally, photocatalysts were prepared by solid-state-reaction (SSR) method which is relatively easy to operate and suitable for large-scale production. However, photocatalytic activity of SSR-products is not high due to the large crystal size and small surface area. Recently, the study of physical and chemical effect of ultrasound irradiation is a rapidly growing research area [17–21]. And the ultrasound gradually becomes an important tool for its applications in the synthesis and modification of nanosized functional inorganic materials. In our previous reports, $BiVO_4$ and Bi_2O_3 nanocrystals were successfully synthesized by a sonochemical route which showed the enhanced photocatalytic activities under visible light for the decomposition of pollutant [22,23].

Herein, we report a new ultrasonic-assisted method for the preparation of Bi_2MO_6 (M = W, Mo) photocatalysts. It was

* Corresponding author. Tel.: +86 21 5241 5295; fax: +86 21 5241 3122.
E-mail address: wzwang@mail.sic.ac.cn (W. Wang).

1381-1169/$ – see front matter © 2006 Elsevier B.V. All rights reserved.
doi:10.1016/j.molcata.2006.12.026

found that ultrasonic irradiation played an important role in the formation of the nanomaterials and final photocatalytic activities. The composition, microstructure, photophysical property and photocatalytic activity of as-prepared products were investigated.

2. Experimental

2.1. Synthesis

All the reagents used in our experiments were of analytical purity and were used as received from Shanghai Chemical Company.

2.1.1. Bi_2WO_6 nanoplates

Aqueous solutions of $Bi(NO_3)_3{\cdot}5H_2O$ and $Na_2WO_4{\cdot}2H_2O$ were mixed together in 1:1 molar ratio, then the mixture was stirred for 30 min at room temperature. Afterward, the mixture was exposed to high-intensity ultrasound (6 mm diameter Ti-horn, 600 W, 20 kHz) irradiation for 60 min. The sonication was conducted without cooling, thus the temperature of the reactant mixture increased gradually and the temperature reached ~70 °C at the end of the reaction. The precipitates were centrifuged, washed with de-ionized water, and then dried at 353 K in air for 10 h. The obtained powders were then calcined at 500 °C for 2 h to produce crystallinity.

2.1.2. Bi_2MoO_6 nanoparticles

All steps were the same as in the synthesis of Bi_2WO_6 nanoplates, except that $(NH_4)_6Mo_7O_{24}{\cdot}4H_2O$ was used instead of $Na_2WO_4{\cdot}2H_2O$.

The samples were also prepared without ultrasonic pretreatment (named as NUS-Bi_2MO_6) while other steps were the same as above. Bulk Bi_2WO_6 and Bi_2MoO_6 were synthesized via traditional solid-state reaction according to Refs. [24,12], respectively.

2.2. Characterization

The powder X-ray diffraction (XRD) patterns of the as-synthesized samples were measured on a D/MAX 2250 V diffractometer (Rigaku, Japan) using monochromatized Cu Kα ($\lambda = 0.15418$ nm) radiation under 40 kV and 100 mA and scanning with the 2θ ranging from 10° to 70°. The morphologies and microstructures of as-prepared samples were examined with transmission electron microscopy (TEM) and high resolution TEM (HRTEM) (JEOL JEM-2100F; accelerating voltage: 200 kV). UV–vis diffuse reflectance spectra of the samples were obtained on an UV–vis spectrophotometer (Hitachi U-3010) using $BaSO_4$ as reference. Nitrogen adsorption–desorption measurements were conducted at 77.35 K on a Micromeritics Tristar 3000 analyzer after samples were degassed at 200 °C for 6 h. The Brunauer–Emmett–Teller (BET) surface area was estimated using adsorption data in a relative pressure range from 0.05 to 0.3.

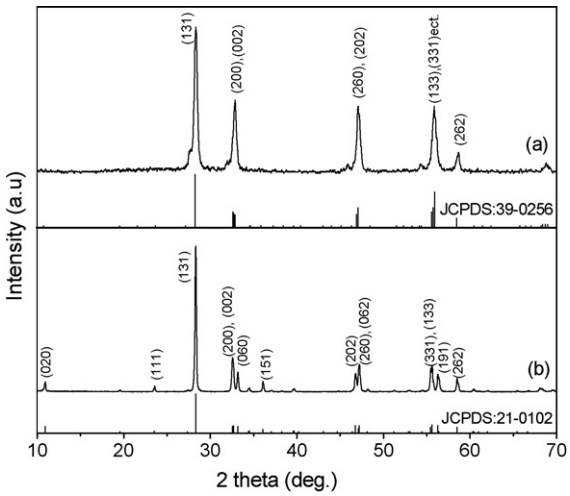

Fig. 1. XRD patterns of as-prepared (a) Bi_2WO_6 and (b) Bi_2MoO_6 powder samples at room temperature, respectively.

2.3. Photocatalytic test

Photocatalytic activities of Bi_2MO_6 samples were evaluated by photocatalytic decolorization of rhodamine-B (RhB) under visible light. A 500 W Xe lamp was used as a light source with a 400 nm cutoff filter to provide visible light irradiation. The experiments were performed at room temperature as follows: 0.1 g of photocatalyst was added into 100 mL RhB solution (10^{-5} mol/L). Before illumination, photocatalyst was stirred for 30 min in the dark to disperse in RhB solution. Then the solution was exposed to visible light irradiation under magnetic stirring. At given time intervals, 3 mL suspensions were sampled and centrifugated to remove the particles. The filtrates of the RhB were monitored by checking the absorbance at 553 nm during the photo-degradation process using Hitachi U-3010 UV–vis spectrophotometer.

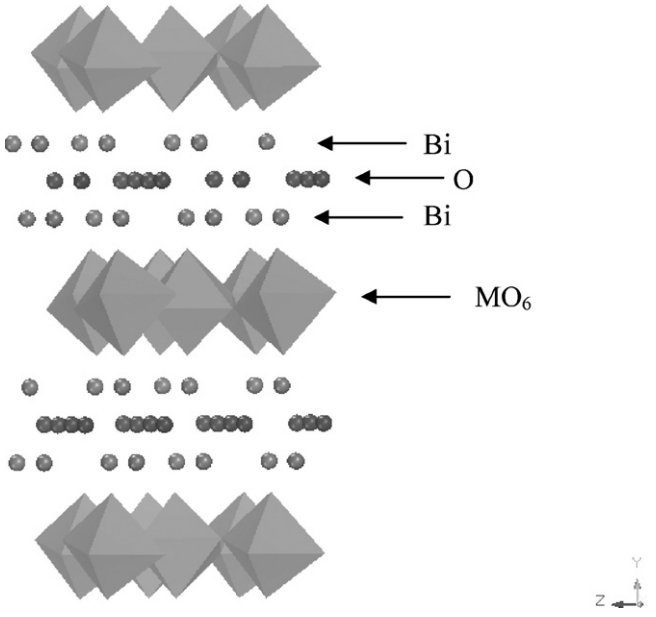

Fig. 2. The schematic crystal structures of orthorhombic phase Bi_2MO_6 (M = W, Mo) composed of MO_6 octahedral layers and Bi–O–Bi layers.

3. Results and discussion

3.1. Crystal structure

The phase and composition of the products were investigated using XRD measurement. Fig. 1 shows the XRD patterns of the Bi_2MO_6 (M = W, Mo) powder samples. All the diffraction peaks can be indexed to orthorhombic Bi_2MO_6 according to the JCPDS card no. 39-0256 for M = W and no. 21-0102 for M = Mo, respectively. After refinement, the crystal lattice parameters were calculated as follows: $a = 5.456$ Å, $b = 16.438$ Å, and $c = 5.441$ Å for Bi_2WO_6, and $a = 5.495$ Å, $b = 16.187$ Å, and $c = 5.486$ Å for Bi_2MoO_6.

Shown in Fig. 2 is schematic crystal structure of Bi_2MO_6. It is a layered structure composed of MO_6 octahedral layers and Bi–O–Bi layers. The samples were crystallized in an orthorhombic system with the space group *Pcba* and $Pna2_1$ for Bi_2WO_6 and Bi_2MoO_6, respectively. The MO_6 octahedral are connected to each other by corner-sharing. It is found that this corner-sharing structure contributed to the visible-light response and the photocatalytic performance of photocatalysts because it makes excitation energy and/or photogenerated electron and hole pairs began to migrate easily [12].

3.2. Morphology and microstructure

The morphology and microstructure of Bi_2MO_6 (M = W, Mo) samples were revealed by TEM. Fig. 3a and b are the TEM images of Bi_2WO_6 sample. The panoramic view shown in Fig. 3a indicates that the as-synthesized products are composed of laminar structure with size of *ca.* 100 nm. Close observation on the samples revealed by high magnification TEM image (Fig. 3b) shows most of these Bi_2WO_6 nanoplates are square-plate-like. The selective area electron diffraction (SAED) pattern of an individual nanoplate (Fig. 3c) shows well-defined ED spots indicating the single-crystal nature of the nanoplate, and the ED pattern can be indexed to the diffraction pattern of [0 1 0] zone axis indicating a preferred (0 1 0) surface orientation of the nanoplates. Fig. 3d shows a typical HRTEM image of a single Bi_2WO_6 nanoplate, and the inset of this figure shows the

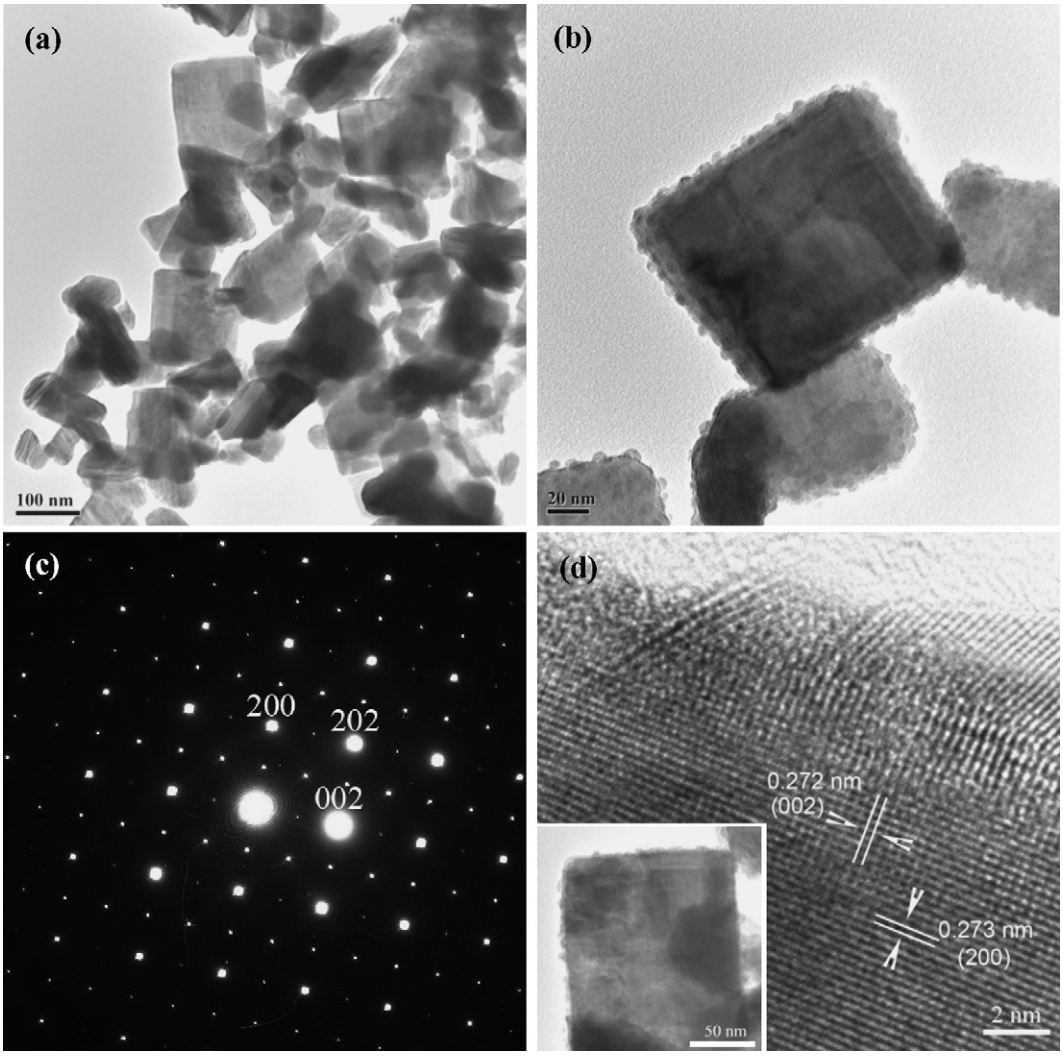

Fig. 3. (a) Low-magnification TEM image of as-synthesized Bi_2WO_6 nanoplates. (b) High-magnification TEM image of a Bi_2WO_6 nanoplate. (c) The corresponding SAED pattern of an individual nanoplate. (d) A HRTEM image near the edge of a single nanoplate (inset).

low-resolution TEM image. The clear lattice fringe indicates the single-crystalline nature of the nanoplate. The observed lattice spacings of 0.272 and 0.273 nm correspond to (0 0 2) and (2 0 0) planes of orthorhombic Bi_2WO_6. This result is in well accordance with that of XRD pattern in Fig. 1a, where the (0 0 2) and (2 0 0) peaks are much stronger compared with those of standard patterns. In addition, under 200 kV electron exposure, the explicit edges gradually became rough and many tiny particles with size of ~5 nm grew from it (Fig. 3b). The phenomenon was also observed by Zhu et al. when they synthesized Bi_2WO_6 nanoplates via a hydrothermal process [11]. The electron beam may create some crater on the basal plane and lead to further stochastic growth on the edge.

Fig. 4a–c are the TEM images of Bi_2MoO_6 sample showing that the product contains a large quantity of nanoparticles with size of *ca*. 150 nm, which is in good agreement with that evaluated using Scherrer equation based on XRD patterns. The SAED pattern (Fig. 4d) recorded on an individual Bi_2MoO_6 nanoparticle reveals the single-crystalline nature of the sample. Unlike Bi_2WO_6 nanoplates mentioned above, Bi_2MoO_6 nanoparticles are stable under 200 kV electron exposure, no visible damage was observed.

The Brunauer–Emmett–Teller (BET) surface areas of Bi_2MO_6 samples were also estimated using N_2 adsorption data. The BET surface areas of samples were estimated to be *ca*. 8.38 m^2/g for Bi_2WO_6 and *ca*. 2.33 m^2/g for Bi_2MoO_6, which was much higher than of the reference SSR-samples of *ca*. 0.64 m^2/g [24] for Bi_2WO_6 and *ca*. 0.9 m^2/g [12] for Bi_2MoO_6. These results demonstrated that Bi_2MO_6 nanocrystals with relatively small crystal size and large surface area could be synthesized, via ultrasonic pretreatment and followed by calcination, as compared with the products of traditional SSR-process.

3.3. UV–vis diffuse reflectance spectra and band gap

The UV–vis diffuse reflectance spectra of the Bi_2MO_6 (M = W, Mo) samples are shown in Fig. 5. The solid-style curve

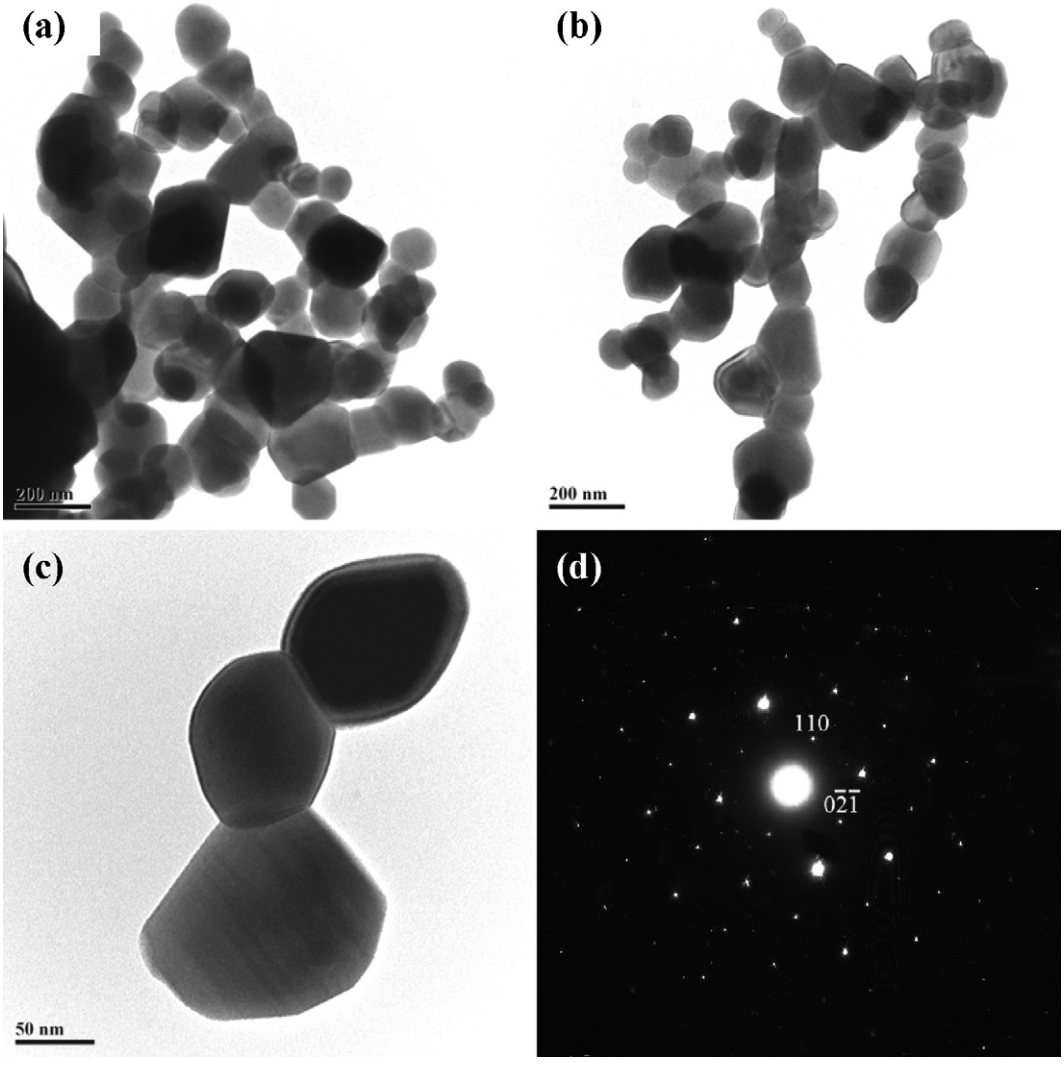

Fig. 4. Low-magnification (a, b) and high-magnification (c) TEM images of as-synthesized Bi_2MoO_6 nanoparticles. (d) The corresponding SAED pattern of an individual nanoparticle.

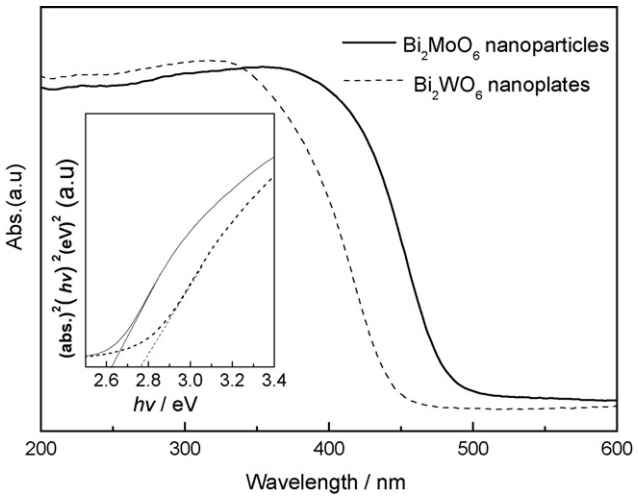

Fig. 5. UV–vis diffuse reflectance spectra of Bi_2WO_6 nanoplates and Bi_2MoO_6 nanoparticles.

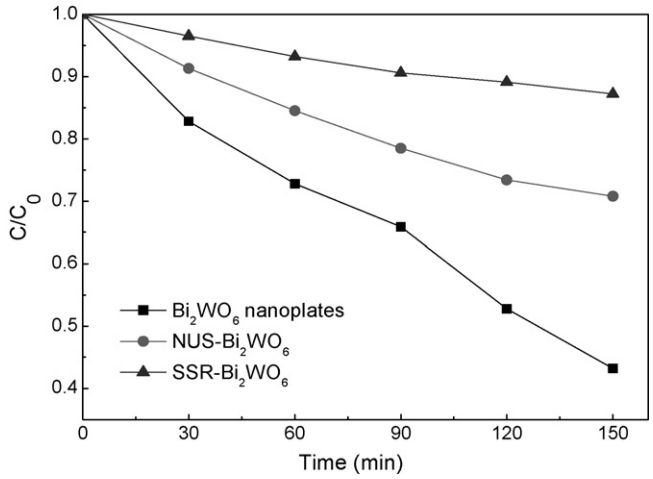

Fig. 6. Photocatalytic degradation of RhB using Bi_2WO_6 nanoplates, SSR-Bi_2WO_6 and the sample without ultrasonic treatment (NUS-Bi_2WO_6) as catalyst ($\lambda > 400$ nm).

represented Bi_2MoO_6 nanoparticles, and the dashed-dotted style curve represented Bi_2WO_6 nanoplate. Both of the samples showed absorption in visible light region in addition to that in the UV light region, which implying the possibility of photocatalytic activity over these materials under visible light irradiation. The steep absorption edge indicating that their absorption relevant to the band gap is due to the intrinsic transition of these semiconductors [25–27]. For a crystalline semiconductor, it is known that the optical absorption near the band edge follows the formula $\alpha h\nu = A(h\nu - E_g)^{n/2}$ [28], where α, h, ν, E_g, and A are absorption coefficient, Planck constant, light frequency, band gap, and a constant, respectively. Among them, n decides the characteristics of the transition in a semiconductor. For Bi_2MO_6, the value of n is 1. The energy of the band gap could be thus estimated to be ~2.77 eV for Bi_2WO_6 nanoplates and ~2.63 eV for Bi_2MoO_6 nanoparticles.

The electronic structure of Bi_2MO_6 have been reported [12,15] based on the DFT calculations. It is revealed that the visible-light response for Bi_2WO_6 was due to the transition from the valence band formed by the hybrid orbitals of Bi 6s and O 2p to the conduction band of W 5d. This special electronic structure makes the VB largely dispersed, which favors the mobility of photo-excitated holes and thus is beneficial to photocatalytic oxidation of organic pollutants [5]. While for Bi_2MoO_6, valence band is only composed of O 2p orbitals. Moreover, the corner-sharing structure of both WO_6 and MoO_6 octahedra contributed to the visible-light response and the photocatalytic performance [12].

3.4. Photocatalytic activities

The photocatalytic activities of Bi_2MO_6 (M = W, Mo) was evaluated by degradation of RhB dye in water under visible light irradiation ($\lambda > 400$ nm). RhB shows a major absorption band at 553 nm. The temporal evolution of the spectral changes taking place during the photodegradation of RhB over Bi_2WO_6 and Bi_2MoO_6 samples were displayed in Figs. 6 and 7, respectively. Under visible light irradiation ($\lambda > 400$ nm), the absorption of RhB/Bi_2MO_6 suspension decreases and the color changes light gradually, indicating the degradation of the dye and removal of ethyl groups [29]. A similar experiment on an aqueous RhB solution in the absence of Bi_2MO_6 photocatalysts was carried out under the same experimental conditions, but the absorption intensity and absorption wavelength hardly changed with increasing irradiation time, as reported previously [30]. In addition, a control experiment also showed that RhB did not degradate in the dark at the presence of photocatalysts. These results confirmed that the degradation of RhB solution is caused by Bi_2MO_6 photocatalysts under visible light irradiation.

For comparison, the same photodegradation experiment using traditional SSR-Bi_2MO_6 and the NUS-Bi_2MO_6 samples were also performed. The results reveal that the photodegradation rates of Bi_2WO_6 nanoplates and Bi_2MoO_6 nanoparticles are evidently higher than that of the corresponding SSR-samples (4–6 times) and the NUS-samples (2–2.4 times). Ultrasonic

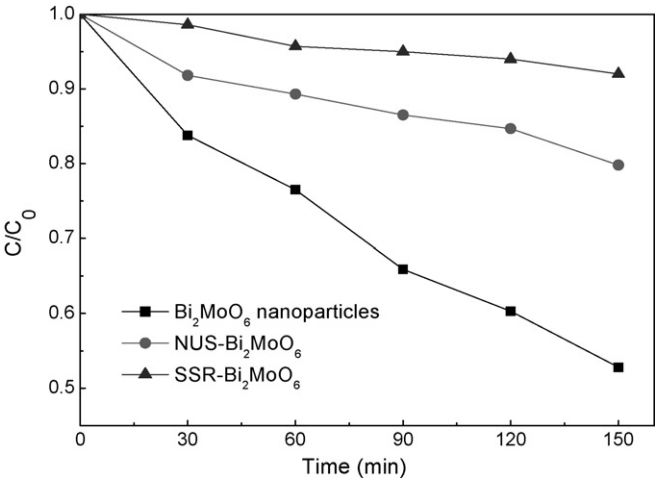

Fig. 7. Photocatalytic degradation of RhB using Bi_2MoO_6 nanoparticles, SSR-Bi_2MoO_6 and the sample without ultrasonic treatment (NUS-Bi_2MoO_6) as catalyst ($\lambda > 400$ nm).

irradiation may play an important role in the formation of the nanomaterials and final photocatalytic activities. The unique chemical effects of ultrasound arise from acoustic cavitation, that is, the ultrasonic vibrations produce microscopic bubbles (cavities), which expand and implode violently, creating millions of shock waves. During the acoustic cavitation process, very high temperatures (>5000 K), pressures (>20 MPa), and cooling rates (>10^{10} K/s) can be achieved upon the collapse of the bubbles [31]. The transient high-temperature and high-pressure field provides a favorable environment for the anisotropic growth of nanocrystals. Cavitations and shock waves created by ultrasound can accelerate solid particles to high velocities leading to interparticle collisions and inducing effective fusion at the point of collision. The energy generated during collision can induce the crystallization of the amorphous particles, responsible for the further crystallization process [32,33]. So we believe it is ultrasound that caused a higher surface area and smaller particle size of the products. A similar result is reported by Yu et al. when they prepared mesoporous titanium dioxide nanocrystalline photocatalyst via ultrasonic process [19]. As compared with that of SSR-samples, the higher photocatalytic activities should relate to the higher surface area of the nanocrystals since the photocatalytic reaction area is increased and the efficiency of the electron-hole separation is promoted [34,35]. Further more, one can see that Bi_2WO_6 nanoplates exhibited higher photocatalytic activities than Bi_2MoO_6 nanoparticles. The result can be ascribed to not only the difference of electronic structure, but also their morphology and surface area. The holes generated inside the Bi_2WO_6 nanoplates had more opportunity to transfer to the surface and act with the organic molecules owe to their thin 2D laminar structure [11].

4. Conclusion

A new ultrasonic-assisted method was developed for the preparation of visible-light-induced Bi_2MO_6 (M = W, Mo) photocatalysts. The as-prepared Bi_2MO_6 nanocrystals exhibited relatively small crystal size and large surface area as compared with the products prepared by traditional solid-state reaction. The Bi_2MO_6 photocatalysts showed much higher (4–6 times) photocatalytic activities under visible light irradiation, as compared with the corresponding sample prepared by traditional solid-state reaction. These higher photocatalytic activities can be ascribed to the morphology, smaller particle size and higher surface areas. Such an ultrasonic-assisted route, as an effective improvement of SSR-process, is worth to be extended to other photocatalysts systems.

Acknowledgements

We acknowledge the financial support from Chinese Academy of Sciences and Shanghai Institute of Ceramics under the program for Recruiting Outstanding Overseas Chinese (Hundred Talents Program), and the National Natural Science Foundation of China (No. 50672117).

References

[1] A. Fujishima, K. Honda, Nature 238 (1972) 37.
[2] M.R. Hoffmann, S.T. Martin, W. Choi, D.W. Bahnemann, Chem. Rev. 95 (1995) 69.
[3] K. Maeda, K. Teramura, D. Lu, T. Takata, N. Saito, Y. Inoue, K. Domen, Nature 440 (2006) 295.
[4] Z. Zou, J. Ye, K. Sayama, H. Arakawa, Nature 414 (2001) 625.
[5] J. Tang, Z. Zou, J. Ye, Angew. Chem., Int. Ed. 43 (2004) 4463.
[6] I. Tsuji, H. Kato, H. Kobayashi, A. Kudo, J. Am. Chem. Soc. 126 (2004) 13406.
[7] I. Tsuji, H. Kato, A. Kudo, Angew. Chem., Int. Ed. 44 (2005) 3565.
[8] K. Maeda, T. Takata, M. Hara, N. Saito, Y. Inoue, H. Kobayashi, K. Domen, J. Am. Chem. Soc. 127 (2005) 8286.
[9] J. Luo, P. Maggard, Adv. Mater. 18 (2006) 514.
[10] H. Tada, T. Mitsui, T. Kiyonaga, T. Akita, K. Tanaka, Nature Mater. 5 (2006) 782.
[11] C. Zhang, Y. Zhu, Chem. Mater. 17 (2005) 3537.
[12] Y. Shimodaira, H. Kato, H. Kobayashi, A. Kudo, J. Phys. Chem. B 110 (2006) 17790.
[13] A. Kudo, S. Hijii, Chem. Lett. 28 (1999) 1103.
[14] J. Yu, A. Kudo, Chem. Lett. 34 (2005) 1528.
[15] H. Fu, C. Pan, W. Yao, Y. Zhu, J. Phys. Chem. B 109 (2005) 22432.
[16] H. Fu, L. Zhang, W. Yao, Y. Zhu, Appl. Catal. B 66 (2006) 100.
[17] A. Gedanken, Ultrason. Sonochem. 11 (2004) 47.
[18] N.A. Dhas, K.S. Suslick, J. Am. Chem. Soc. 127 (2005) 2368.
[19] J.G. Yu, M.H. Zhou, B. Cheng, H.G. Yu, X.J. Zhao, J. Mol. Catal. A 227 (2005) 75.
[20] X.F. Qiu, C. Burda, R.L. Fu, L. Pu, H.Y. Chen, J.J. Zhu, J. Am. Chem. Soc. 126 (2004) 16276.
[21] W. Ho, J. Yu, J. Mol. Catal. A 247 (2006) 268.
[22] L. Zhou, W. Wang, S. Liu, L. Zhang, H. Xu, W. Zhu, J. Mol. Catal. A 252 (2006) 120.
[23] L. Zhang, W. Wang, J. Yang, Z. Chen, W. Zhang, L. Zhou, S. Liu, Appl. Catal. A 308 (2006) 105.
[24] J. Tang, Z. Zou, J. Ye, Catal. Lett. 92 (2004) 53.
[25] S. Zhang, C. Zhang, Y. Man, Y. Zhu, J. Solid State Chem. 179 (2006) 62.
[26] J. Yin, Z. Zou, J. Ye, J. Phys. Chem. B 107 (2003) 4936.
[27] J. Tang, Z. Zou, J. Ye, J. Phys. Chem. B 107 (2003) 14265.
[28] M.A. Butler, J. Appl. Phys. 48 (1977) 1914.
[29] W. Zhao, C. Chen, X. Li, J. Zhao, J. Phys. Chem. B 106 (2002) 5022.
[30] T. Wu, G. Liu, J. Zhao, J. Phys. Chem. B 102 (1998) 5845.
[31] K.S. Suslick, S.B. Choe, A.A. Cichowlas, M.W. Grinstaff, Nature 353 (1991) 414.
[32] S.J. Doktycz, K.S. Suslick, Science 247 (1990) 1067.
[33] J. Geng, J. Zhu, H. Chen, Cryst. Growth Des. 6 (2006) 321.
[34] D. Wang, J. Tang, Z. Zou, J. Ye, Chem. Mater. 17 (2005) 5177.
[35] J. Yu, J. Xiong, B. Cheng, S. Liu, Appl. Catal. B 60 (2005) 211.